Low Beam Energy X-Ray Microanalysis

J. Goldstein et al., *Scanning Electron Microscopy and X-Ray Microanalysis*,
https://doi.org/10.1007/978-1-4939-6676-9_22

22.1 What Constitutes "Low" Beam Energy X-Ray Microanalysis?

The incident beam energy, E_0, is the parameter that determines which characteristic X-rays can be excited: the beam energy must exceed the critical excitation energy, E_c, for an atomic shell to initiate ionization and subsequent emission of characteristic X-rays. This dependence is parameterized with the "overvoltage" $U_{0,}$ defined as

$$U_0 = E_0 / E_c \tag{22.1}$$

U_0 must exceed unity for X-ray emission. The intensity, I_{ch}, of characteristic X-ray generation follows an exponential relation:

$$I_{ch} = i_B a (U_0 - 1)^n \tag{22.2}$$

where i_B is the beam current, a and n are constants, with $1.5 \leq n \leq 2$.

The intensity of the X-ray continuum (*bremsstrahlung*), I_{cm}, also depends on the incident beam energy:

$$I_{cm} = i_B b Z (U_0 - 1) \tag{22.3}$$

where b is a constant and Z is the mass-concentration-averaged atomic number of the specimen.

The peak-to-background is then obtained as the ratio of Eqs. (22.2) and (22.3):

$$P / B = I_{ch} / I_{cm} \approx (1/Z)(U_0 - 1)^{n-1} \tag{22.4}$$

The value of $n - 1$ in Eq. (22.4) ranges from 0.5 to 1, so that the P/B rises slowly as U_0 increases above unity. ◘ Figure 22.1 shows experimental measurements of Si K-L_2 + Si K-M_3 (Si Kα,β) characteristic X-ray intensity as a function of overvoltage. Near the threshold of $U_0 = 1$, the intensity drops sharply, and the Si K-L_2 + Si K-M_3 peak becomes progressively lower relative to the X-ray continuum background, as shown in ◘ Fig. 22.2 for Si measured over a range of beam energies. The peak-to-background strongly influences the limit-of-detection. While X-ray measurements can certainly be made with $1 < U_0 < 1.25$ and the limit-of-detection can be improved by increasing the integrated spectrum intensity by extending the counting time, the detectability within a practical measuring time of a constituent excited in this overvoltage range diminishes. While major constituents may be detected, minor and trace constituents are likely to be below the limit of detection. Thus the situation for $1 < U_0 < 1.25$ must generally be considered "marginally detectable" and is so marked in ◘ Figs. 22.3, 22.4, 22.5, 22.6, 22.7, and 22.8.

◘ Fig. 22.1 Production of silicon K-shell X-rays with overvoltage

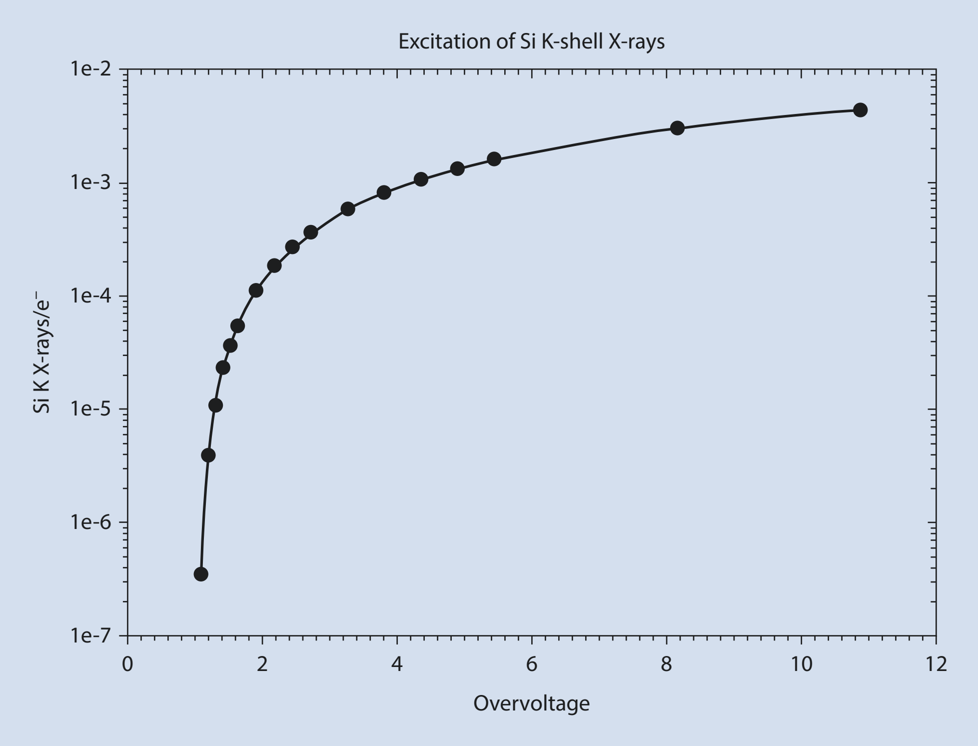

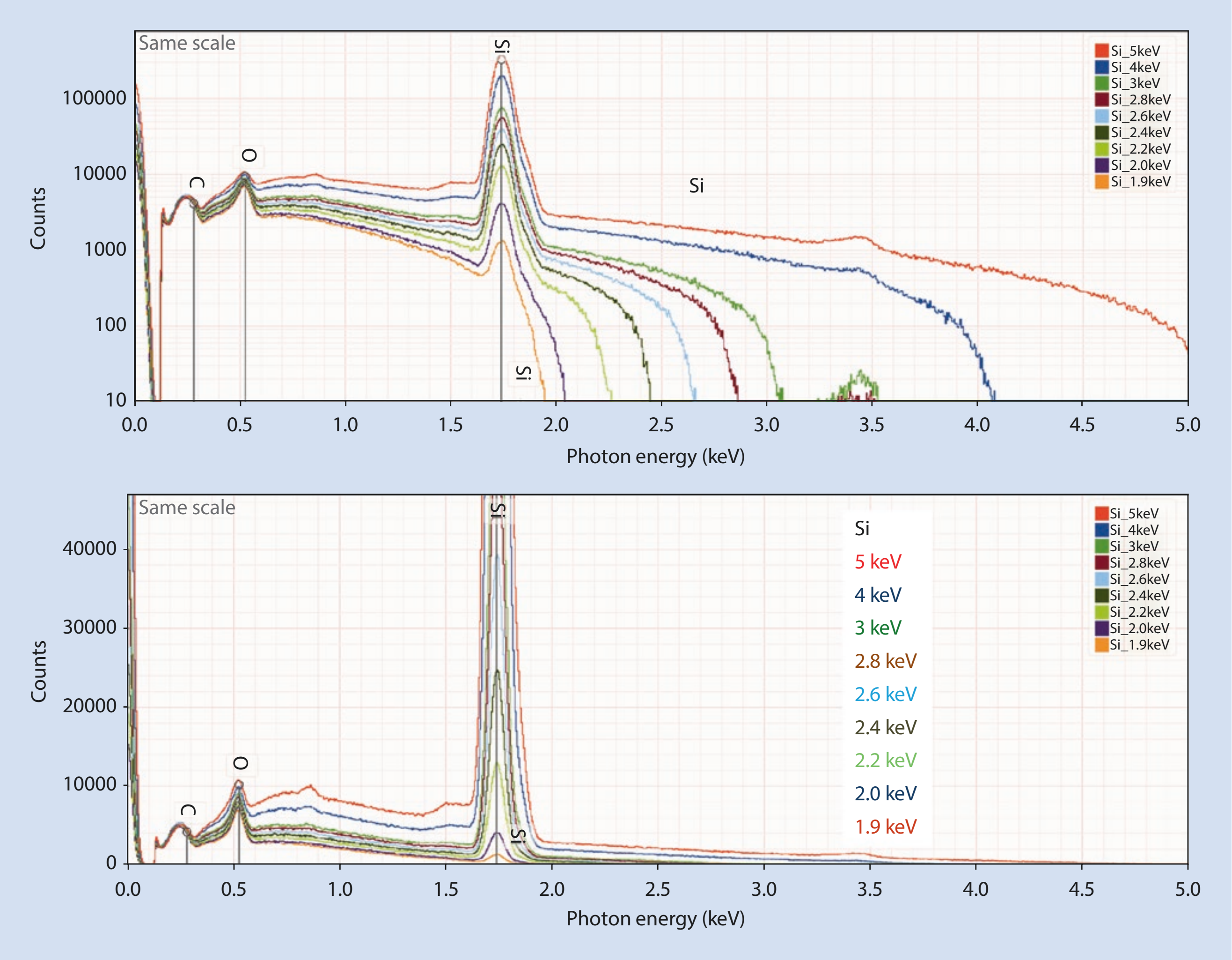

Fig. 22.2 Silicon at various incident beam energies from 5 keV to 1.9 keV showing the decrease in the peak-to-background with decreasing overvoltage

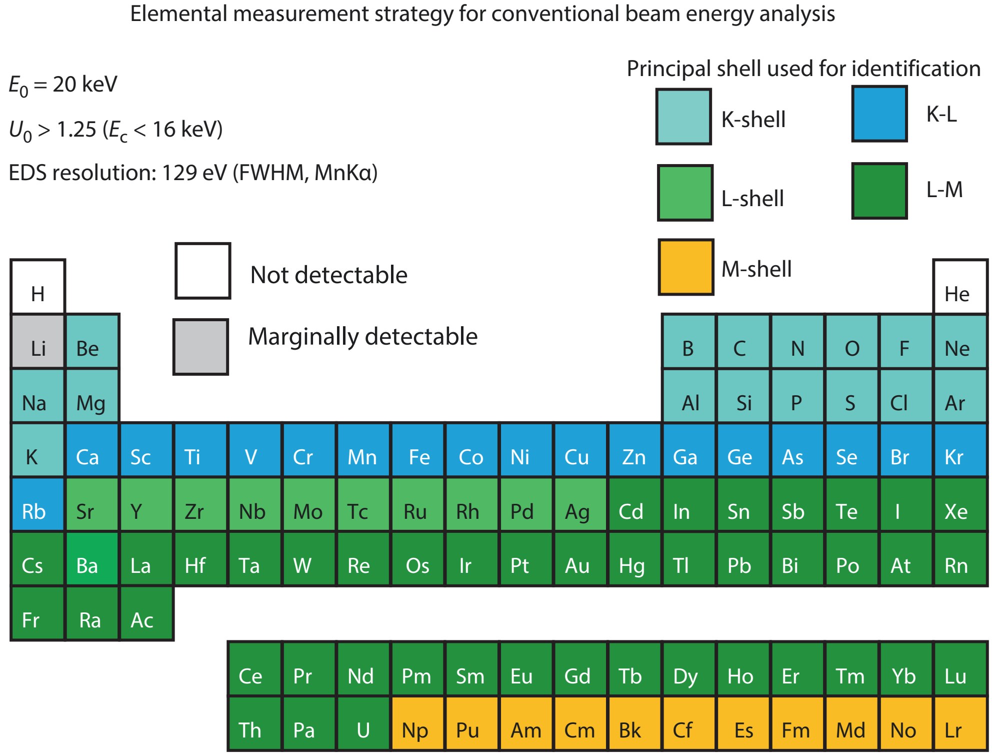

Fig. 22.3 Periodic table illustrating X-ray shell choices for developing analysis strategy within the conventional beam energy range, $E_0 = 20$ keV (Newbury and Ritchie, 2016)

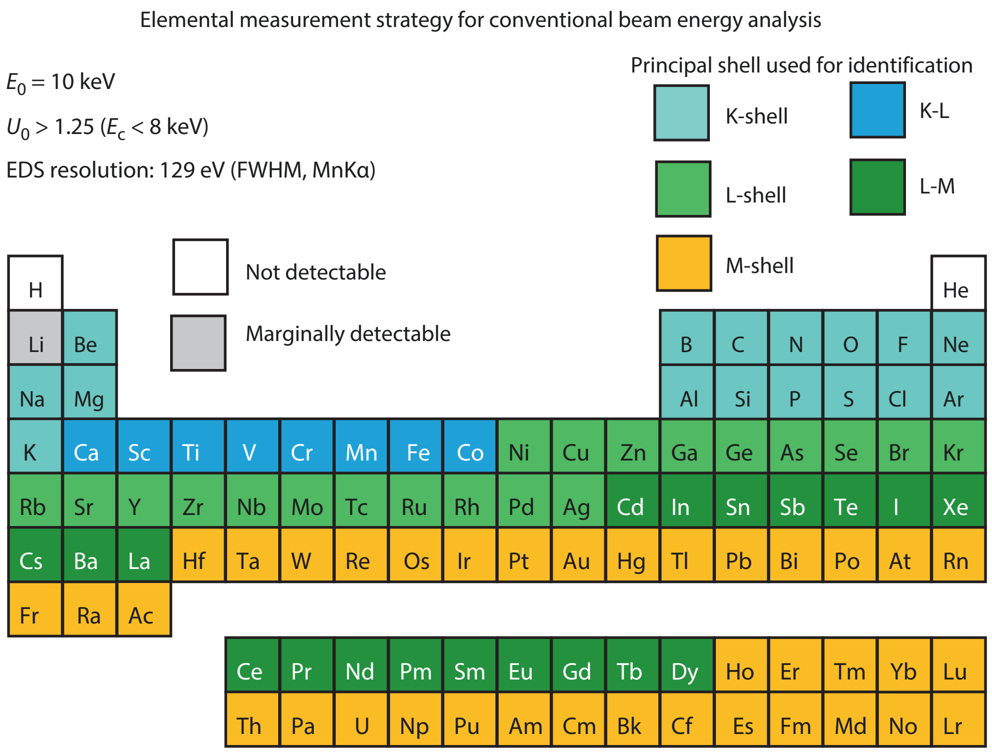

Fig. 22.4 Periodic table illustrating X-ray shell choices for developing analysis strategy at the lower end of the conventional beam energy range, $E_0 = 10$ keV (Newbury and Ritchie, 2016)

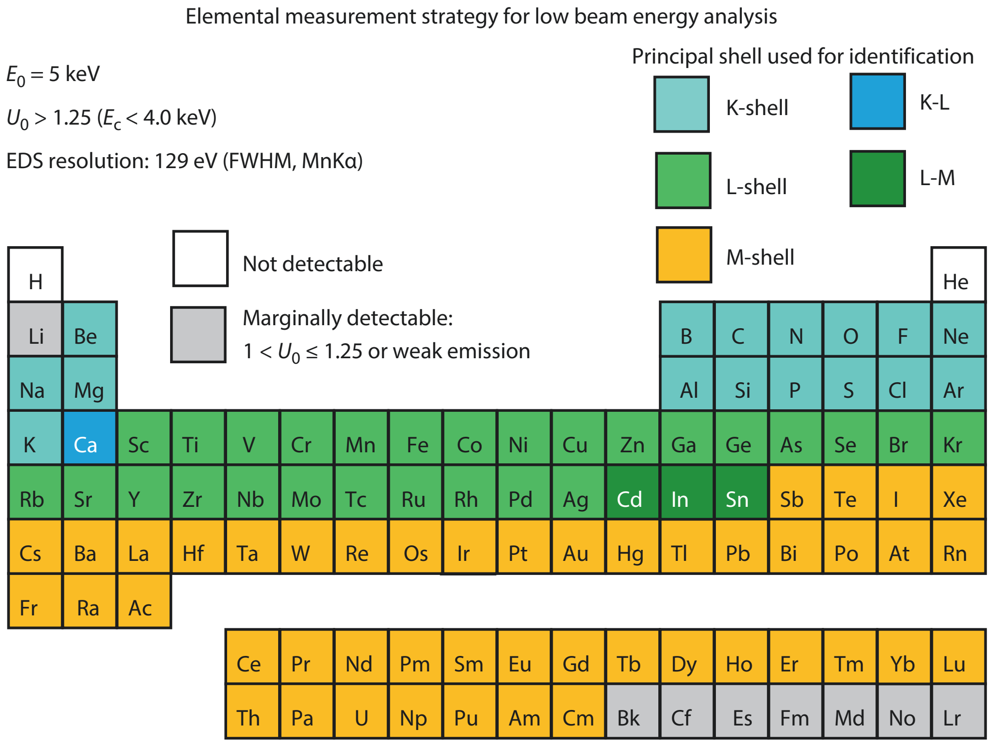

Fig. 22.5 Periodic table illustrating X-ray shell choices for developing analysis strategy for the upper end of the low beam energy range, $E_0 = 5$ keV (Newbury and Ritchie, 2016)

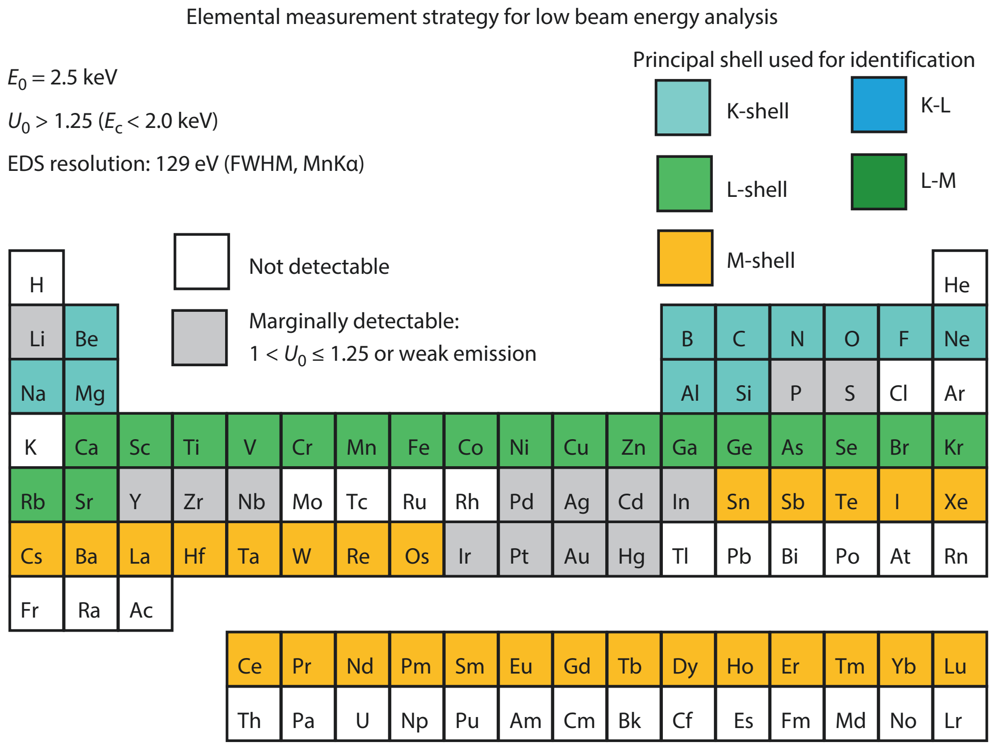

Fig. 22.6 Periodic table illustrating X-ray shell choices for developing analysis strategy within the low beam energy range, $E_0 = 2.5$ keV (Newbury and Ritchie, 2016)

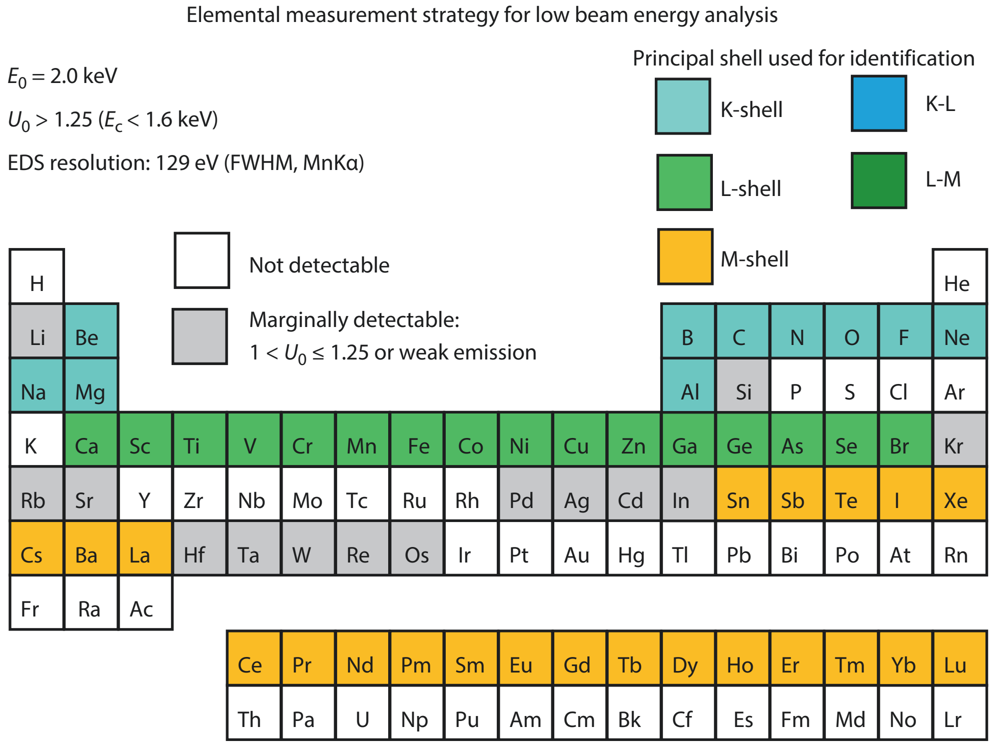

Fig. 22.7 Periodic table illustrating X-ray shell choices for developing analysis strategy within the low beam energy range, $E_0 = 2.0$ keV (Newbury and Ritchie, 2016)

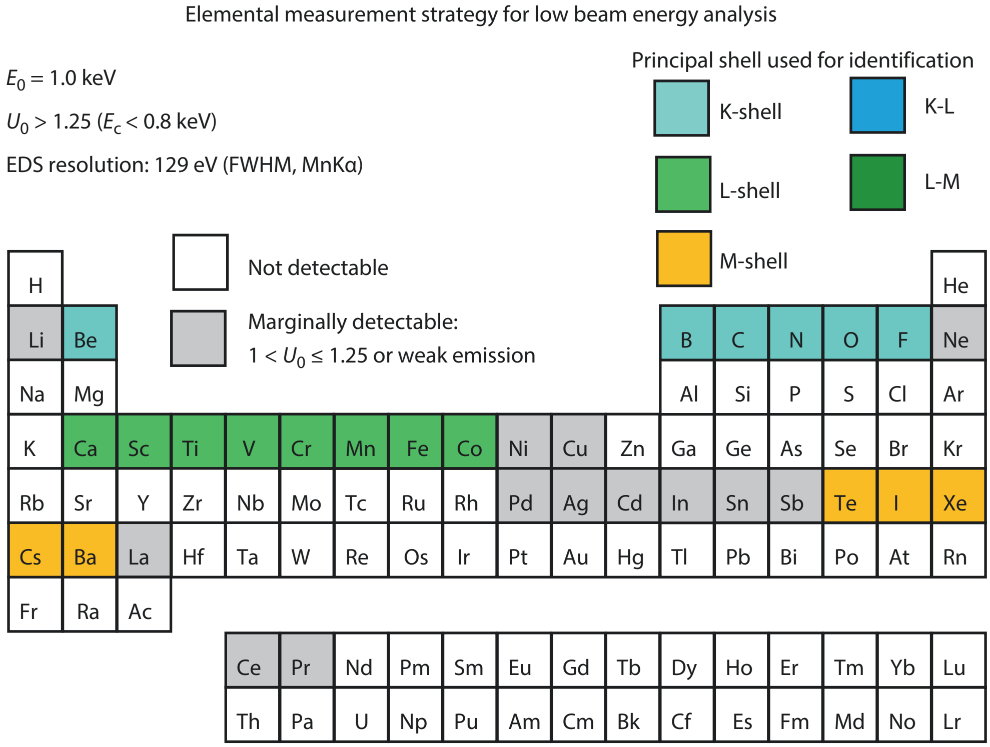

Fig. 22.8 Periodic table illustrating X-ray shell choices for developing analysis strategy within the low beam energy range, $E_0 = 1.0$ keV (Newbury and Ritchie, 2016)

22.1.1 Characteristic X-ray Peak Selection Strategy for Analysis

"Conventional" electron-excited X-ray microanalysis is typically performed with an incident beam energy selected between 10 keV and 30 keV. A beam energy is this range is capable of exciting X-rays from one or more atomic shells for all elements of the periodic table, except for hydrogen and helium, which do not produce characteristic X-ray emission. Li can produce X-ray emissions, but the energy of 0.052 keV is below the practical detection limit of most EDS systems, which typically have a threshold of approximately 0.1 keV. Recent progress in silicon drift detector (SDD)-EDS detector technology and isolation windows is rapidly improving the EDS performance in the photon energy range 50 eV – 250 eV, raising the measurement situation for Li from "undetectable" to the level of "marginally detectable." The choices available for the characteristic X-ray peaks to analyze various elements are illustrated in the periodic table shown in Fig. 22.3 for $E_0 = 20$ keV. In constructing this diagram, the assumption has been made with the requirement that $U_0 > 1.25$ ($E_c < 16$ keV) to provide for robust detection of major and minor constituents. Note that in constructing Fig. 22.3, only the excitation of characteristic X-rays has been considered and not the subsequent absorption of X-rays during propagation through the specimen to reach the detector. Absorption has a strong effect on low energy X-rays below 2-keV photon energy and strongly depends on composition and beam energy. Absorption can be minimized by operating at low beam energy, as discussed below, an important factor that must also be considered when developing practical X-ray measurement strategy.

As seen in Fig. 22.3, when the beam energy is selected at the high end of the conventional range, X-rays from two different atomic shells can be excited for many elements, and the additional information provided by having two X-ray families with two or more peaks to identify greatly increases the confidence that can be placed in an elemental identification. This is especially valuable when peak interference occurs between two elements. For example, a severe interference occurs between S K-$L_{2,3}$ (2.307 keV) and Mo L_3-$M_{4,5}$ (2.293 keV), which are separated by 14 eV. To confirm the presence of Mo when S may also be present, operation with $E_0 > 25$ keV ($U_0 = 1.25$) will also excite Mo K-$L_{2,3}$ (17.48 keV) for unambiguous identification of Mo.

When the beam energy is lowered to the bottom of the conventional analysis range, $E_0 = 10$ keV, the available X-ray shells for measurement are reduced as shown in Fig. 22.4. Many more elements can only be analyzed with X-rays from one shell, for example, the Ni to Rb L-shells and the Hf to U M-shells.

22.1.2 Low Beam Energy Analysis Range

When the incident beam energy is reduced to $E_0 = 5$ keV, further reduction in the atomic shells that can be excited creates the situation shown in ◘ Fig. 22.5. At 5 keV, only one shell is available for all elements except Ca, Cd, In, and Sn. When the incident energy is reduced below 5 keV, some elements are effectively rendered analytically inaccessible by the restrictions imposed by the X-ray physics. The progressive loss of access to elements in the periodic table is illustrated for $E_0 = 2.5$ keV (◘ Fig. 22.6), $E_0 = 2$ keV (◘ Fig. 22.7), and $E_0 = 1$ keV (◘ Fig. 22.8). Indeed, even with $E_0 = 5$ keV, several elements must be measured with X-rays from shells with low fluorescence yield, such as the Ti L-family and the Ba M-family, resulting in poor peak-to-background.

Based upon the restrictions imposed by the physics of X-ray generation, $E_0 = 5$ keV is the lowest energy which still gives access to the full periodic table, except for H and He, and therefore this value will be considered as the upper bound of the beam energy range for low beam energy microanalysis. The beam energy range from 5 keV to 10 keV represents the transition region between low beam energy microanalysis and conventional X-ray microanalysis.

22.2 Advantage of Low Beam Energy X-Ray Microanalysis

22.2.1 Improved Spatial Resolution

The spatial resolution of X-ray microanalysis is controlled by the range of the electrons for the excitation of characteristic X-rays, as described by the Kanaya–Okayama (1974) range equation modified for the threshold of X-ray production set by the critical excitation energy:

$$R_{\mathrm{K-O}}\left(\mu\mathrm{m}\right) = \left(0.0276\,A / Z^{0.89}\rho\right)\left(E_0^{\,1.67} - E_c^{\,1.67}\right) \qquad \mathbf{(22.5)}$$

where A (g/mol) is the atomic weight, Z is the atomic number, ρ (g/cm^3) is the density, E_0 (keV) is the beam energy and E_c (keV) is the shell ionization energy. ◘ Figure 22.9 shows the range for the production of Na K-shell X-rays in various matrices: C, Al, Ti, Fe, Ag, and Au. For low beam energy analysis conditions, the range at $E_0 = 5$ keV varies from 0.46 µm (460 nm) for Na in a C matrix to 0.08 µm (80 nm) in

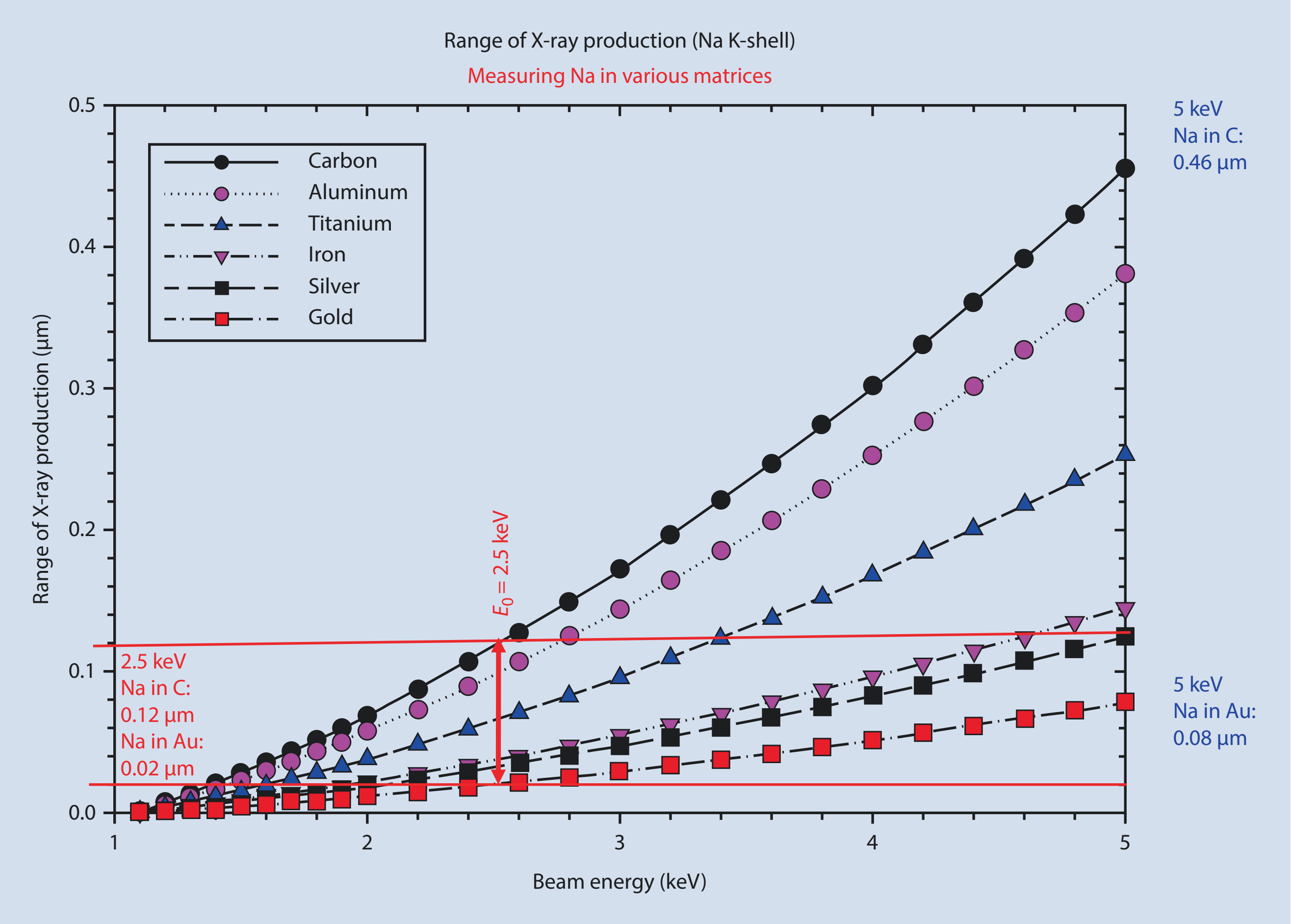

◘ **Fig. 22.9** Range of production of Na K-shell X-rays in various matrices, as calculated with the Kanaya–Okayama range equation

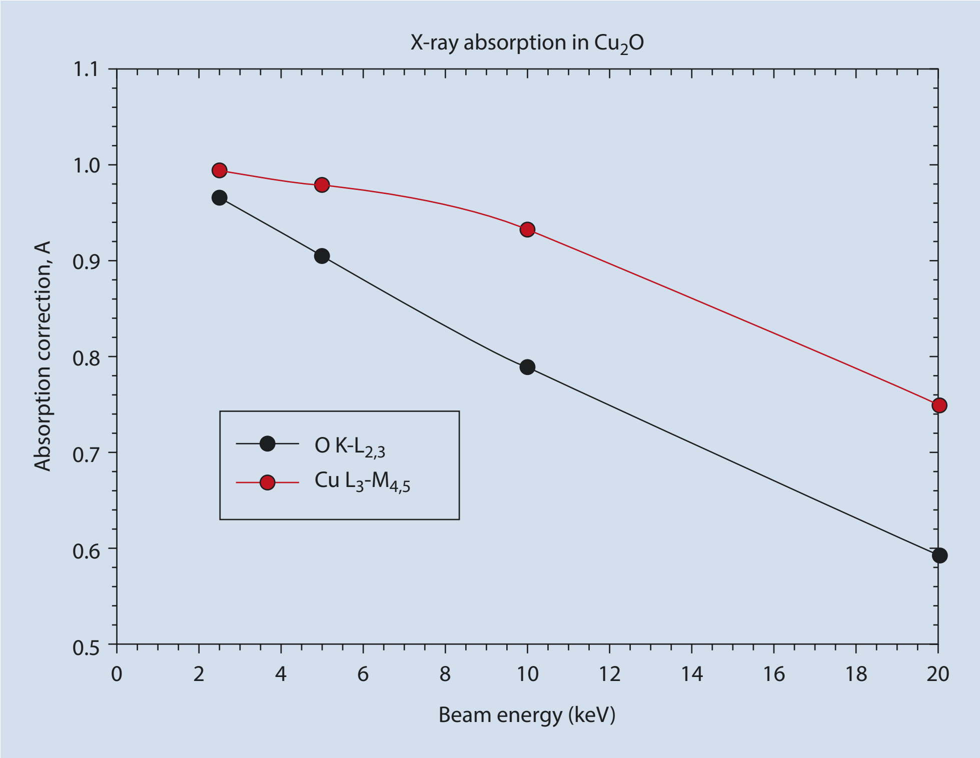

Fig. 22.10 Absorption correction factor for O K-$L_{2,3}$ (relative to MgO) and Cu L_3-$M_{4,5}$ (relative to Cu) as a function of beam energy

Au, while at $E_0 = 2.5$ keV, the range for Na collapses to 0.12 µm (120 nm) in a C matrix to 0.02 µm (20 nm) in Au.

22.2.2 Reduced Matrix Absorption Correction

When the range of X-ray production is reduced by lowering the beam energy, the generated X-rays undergo lower absorption because of the reduced path length to the surface. This can be a strong effect, because X-ray absorption follows an exponential relationship:

$$I / I_0 = exp\left[-(\mu / \rho)\rho s\right] \tag{22.6}$$

where I_0 is the original intensity and I is the intensity remaining after passing through a distance s (cm) of a material of density ρ (g/cm^3) and of mass absorption coefficient, μ/ρ (cm^2/g). For strongly absorbed photons, which is typically the case for low energy photons, the matrix correction for absorption diminishes rapidly (i.e., approaches unity) as the beam energy is reduced, as shown in Fig. 22.10 for O K-$L_{2,3}$ and Cu L_3-$M_{4,5}$ in Cu_2O (measured relative to MgO and Cu).

22.2.3 Accurate Analysis of Low Atomic Number Elements at Low Beam Energy

Low atomic number elements with $Z \leq 10$ have characteristic X-ray energies below 1 keV, and these low energy photons suffer especially high absorption. By minimizing absorption through operation at low beam energy, Li and Be can be detected; and B, C, N, and F, can be quantitatively analyzed with accuracy such that the analyzed value is generally within ±5 % relative to the true value, as presented in Table 22.1 (borides), Table 22.2 (carbides), Table 22.3

Table 22.1 Analysis of metal borides at $E_0 = 5$ keV (5 replicates); atomic concentrations

Compound	Metal, C_{av}	Relative accuracy,%	σ_{rel}, %	Boron, C_{av}	Relative accuracy,%	σ_{rel}, %
CrB_2	0.3482	4.5	0.32	0.6518	−2.2	0.17
CrB	0.5149	3.0	0.17	0.4851	−3.0	0.19
Cr_2B	0.6769	1.5	0.65	0.3231	−3.1	1.4
TiB_2	0.3373	1.2	3.6	0.6627	−0.6	1.8

Table 22.2 Analysis of metal carbides at $E_0 = 5$ keV (5 replicates); atomic concentrations

Compound	Metal, C_{av}	Relative accuracy,%	σ_{rel}, %	Carbon, C_{av}	Relative accuracy,%	σ_{rel}, %
SiC	0.4935	−1.3	0.25	0.5065	1.3	0.25
Cr_3C_2	0.6002	0.03	1.4	0.3998	−0.05	2
Fe_3C	0.7479	−0.28	0.23	0.2521	0.84	0.67
ZrC	0.5025	0.49	1.2	0.4975	−0.49	1.2

Table 22.3 Analysis of metal nitrides at $E_0 = 5$ keV (5 replicates); atomic concentrations

Compound	Metal, C_{av}	Relative accuracy,%	σ_{rel}, %	Nitrogen, C_{av}	Relative accuracy,%	σ_{rel}, %
TiN	0.5168	3.4	0.30	0.4832	−3.4	0.32
Cr_2N	0.6606	−0.91	0.55	0.3394	1.8	1.1
Fe_3N	0.7413	−1.1	2	0.2587	3.5	5.7
HfN	0.5050	1.0	1.4	0.495	−1.0	1.4

Table 22.4 Analysis of metal oxides at $E_0 = 5$ keV (5 replicates); atomic concentrations

Compound	Metal, C_{av}	Relative accuracy,%	σ_{rel}, %	Oxygen, C_{av}	Relative accuracy,%	σ_{rel}, %
TiO_2	0.3299	−1.0	0.34	0.6701	0.5	0.17
NiO	0.5110	2.2	0.30	0.4890	−2.2	0.34
CuO	0.5105	2.1	0.10	0.4895	−2.1	0.11
Cu_2O	0.6815	2.2	0.13	0.3185	−4.4	0.28

(nitrides), and Table 22.4 (oxides) (Newbury and Ritchie 2015). Examples of EDS spectra and the residual spectrum after fitting are shown in Fig. 22.11 (Cr borides), Fig. 22.12 (Cr_3C_2), Fig. 22.13 (Fe_3N), and Fig. 22.14 (Cu oxides). These examples of analyses for low atomic number elements in compounds with NIST DTSA II used pure elements and stoichiometric compounds (MgO, GaN) as peak-fitting references and standards. Note that with the exception of the Si K-family, the L-shell and M-shell characteristic X-rays of the metallic elements were used as the analytical peaks because the low beam energy was not adequate to ionize the K-shells of these elements (Ti, Cr, Fe, Ni, Cu, Zr).

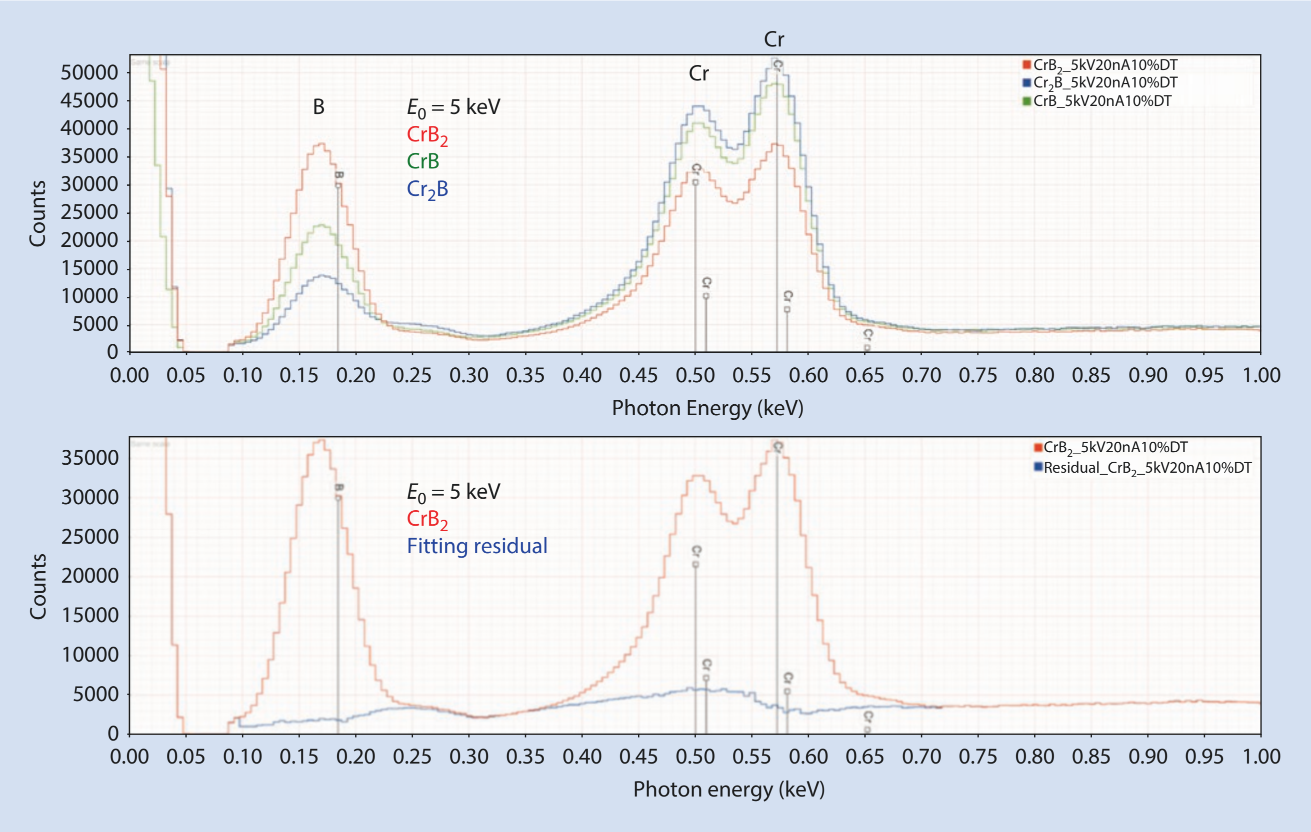

Fig. 22.11 EDS spectra of chromium borides: CrB2, CrB and Cr_2B (upper) and residual after peak fitting for B and Cr in CrB_2 (lower); $E_0 = 5$ keV

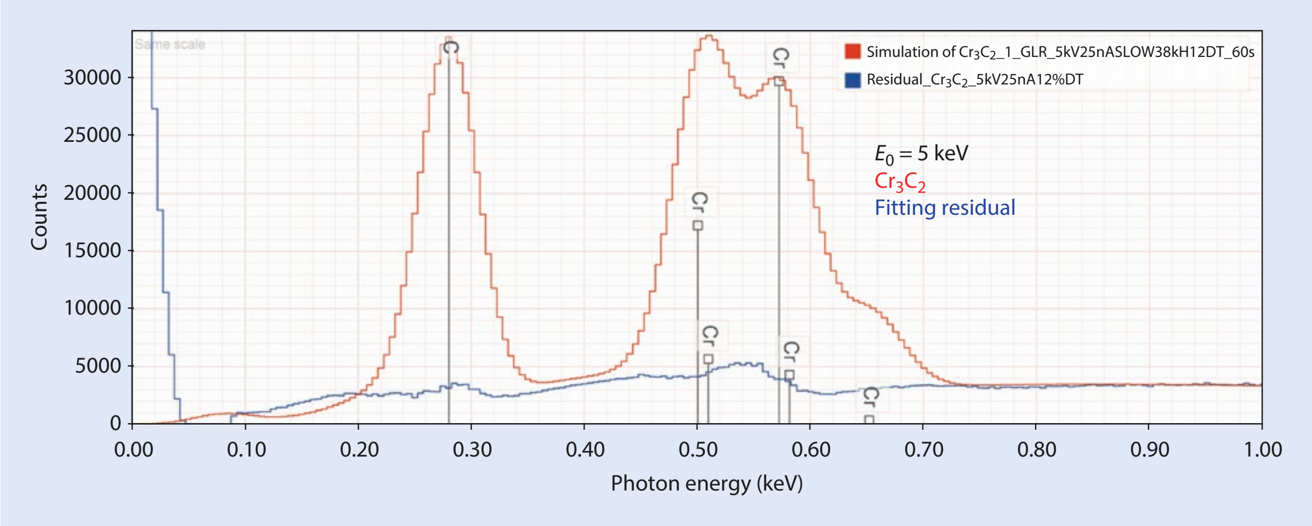

Fig. 22.12 EDS spectrum of chromium carbide, Cr_3C_2 and residual after peak fitting for C and Cr; $E_0 = 5$ keV

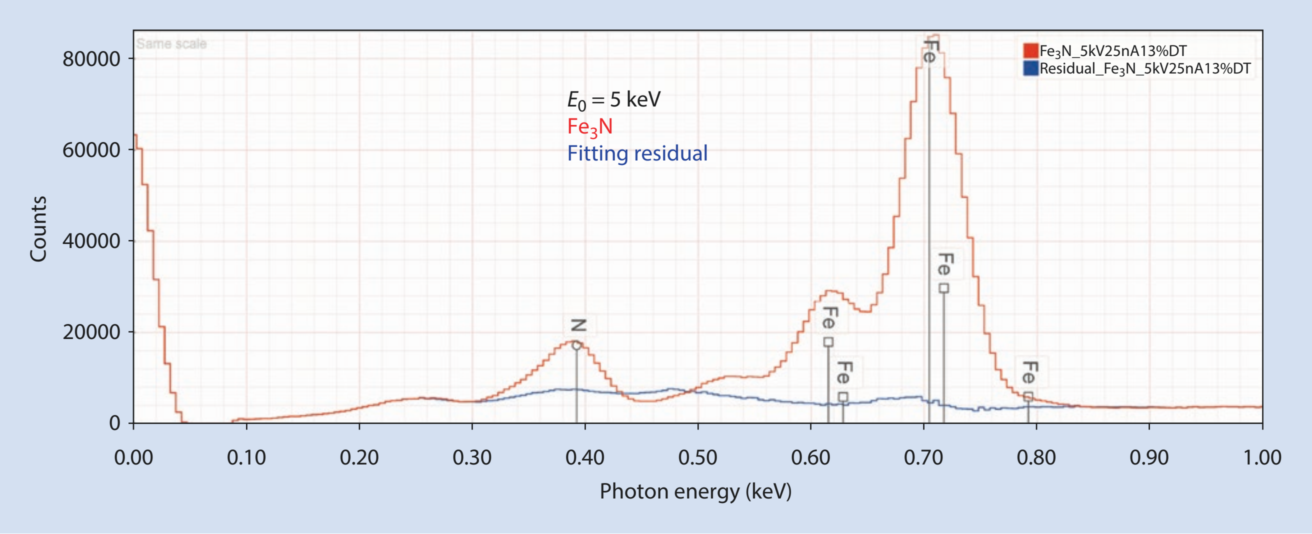

Fig. 22.13 EDS spectrum of iron nitride, Fe_3N and residual after peak fitting for N and Fe; $E_0 = 5$ keV

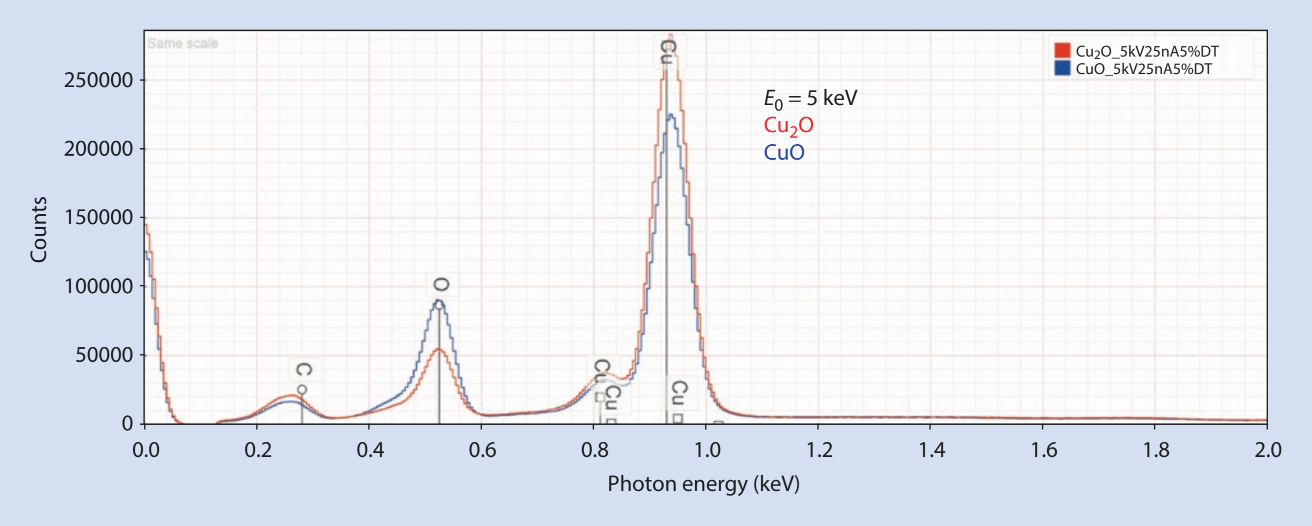

Fig. 22.14 EDS spectra of copper oxides, Cu_2O and CuO; $E_0 = 5$ keV

22.3 Challenges and Limitations of Low Beam Energy X-Ray Microanalysis

22.3.1 Reduced Access to Elements

High performance SEMs can routinely operate with the beam energy as low as 500 eV; and with special electron optics and/or stage biasing, the landing kinetic energy of the beam can be reduced to 10 eV. Because the beam penetration depth decreases rapidly as the incident energy is reduced, as shown in Fig. 22.9, which plots the Kanaya–Okayama range for 0 – 5 keV, low kinetic energy provides extreme sensitivity to the surface of the specimen, which can improve the contrast from surface features of interest. Since the lateral ranges over which the backscattered electron (BSE) and closely related SE_2 signals are emitted are also greatly restricted at low beam energies, these signals closely approach the beam footprint of SE_1 emission and thus contribute to high spatial resolution imaging rather than degrading resolution as they do at high beam energy. Thus, low beam energy operation has strong advantages for SEM imaging down to beam landing energies of tens of eV.

While low beam energy SEM imaging can exploit the full range of landing kinetic energies to seek to maximize contrast from surface features of interest, the situation for low beam energy X-ray microanalysis is much more constrained. As discussed above, as the beam energy is reduced, the atomic shells that can be ionized become more restricted. A beam energy of 5 keV is the lowest energy that provides access to measureable X-rays for elements of the periodic table from $Z = 3$ (Li) to $Z = 94$ (Pu), as shown in ▣ Fig. 22.5. If the beam energy is reduced to $E_0 = 2.5$ keV, EDS X-ray microanalysis of large portions of the periodic table is no longer possible because no atomic shell with useful X-ray yield can be excited or effectively measured for these elements, creating the situation shown in ▣ Fig. 22.6. Further decreases in the beam energy results in losing access to even more elements, with only about half of the elements measureable at $E_0 = 1$ keV, and many of those only marginally so.

Even to achieve the elemental coverage depicted for $E_0 = 5$ keV in ▣ Fig. 22.5, low beam energy EDS X-ray microanalysis requires measurement of characteristic X-rays that are not normally utilized in conventional beam energy analysis for certain elements. Thus Ti must be measured with the Ti L-family when $E_0 \leq 5$ keV, as shown in ▣ Fig. 22.15. Similarly, for Ba, the Ba L-family around 4.5 keV is the usual choice for microanalysis, but the Ba L_3 excitation energy is 5.25 keV, and thus the Ba L-family not excited with $E_0 = 5$ keV, forcing the analyst to utilize the Ba M-family. The EDS spectrum of $BaCl_2$ with $E_0 = 5$ keV is shown in ▣ Fig. 22.16. Due to the low fluorescence yield of ionizations in the Ba M-shell, the Ba M-family peaks are seen to have a relatively low peak-to-background, despite Ba being present in this case as a major constituent (mass concentration $C = 0.696$), making the measurement of Ba when present as a minor to trace constituent even more problematic. A practical problem that arises when analyzing with the Ba M-family peaks is the difficulty in obtaining suitable Ba M-family peak references that are free of interferences from other elements. While $BaCl_2$ is interference-free in the Ba M-family region, BaF_2 and $BaCO_3$ are not, as shown in ▣ Fig. 22.16. However, $BaCl_2$ shows evidence of degradation under the electron beam, possibly changing the local compositions and thus disqualifying it as a standard. Despite degradation under the beam, $BaCl_2$ can serve as a peak reference, while BaF_2 or another Ba-containing compound or glass that is stable under electron bombardment can serve as a standard. Despite these challenges, successful analysis of the high transition temperature superconducting material $YBa_2Cu_3O_{7-X}$ at $E_0 = 2.5$ keV with CuO, Y_2O_3, and BaF_2 as the standard and $BaCl_2$ as the peak reference is demonstrated in ▣ Fig. 22.17 and ▣ Table 22.5, where analyses with oxygen done directly against a standard (ZnO) and by the method of assumed oxygen stoichiometry of the cations are presented.

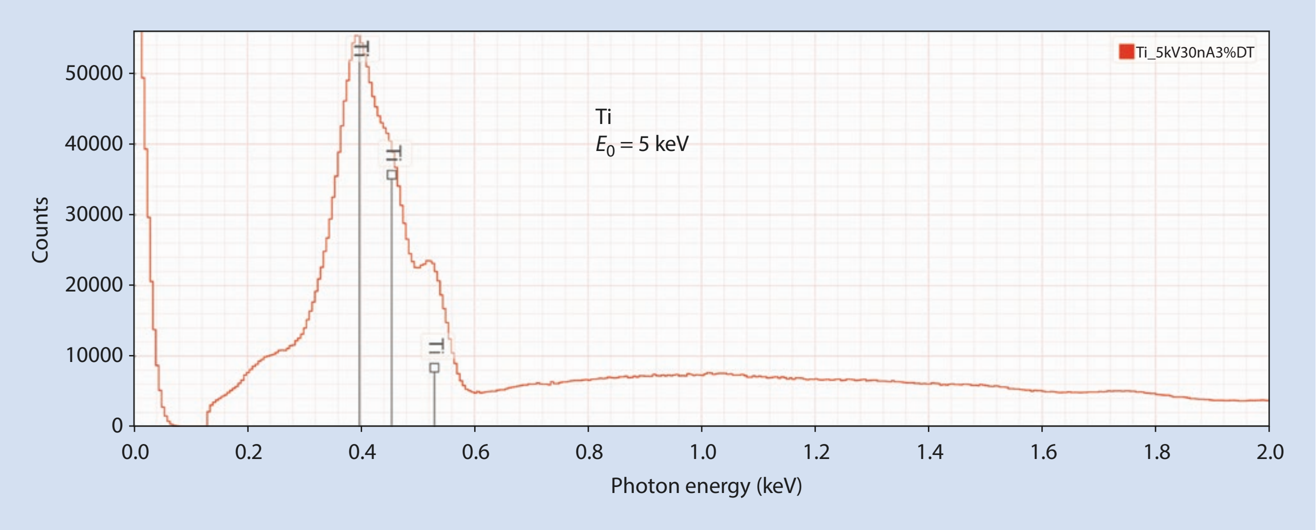

▣ **Fig. 22.15** EDS spectrum of titanium; $E_0 = 5$ keV

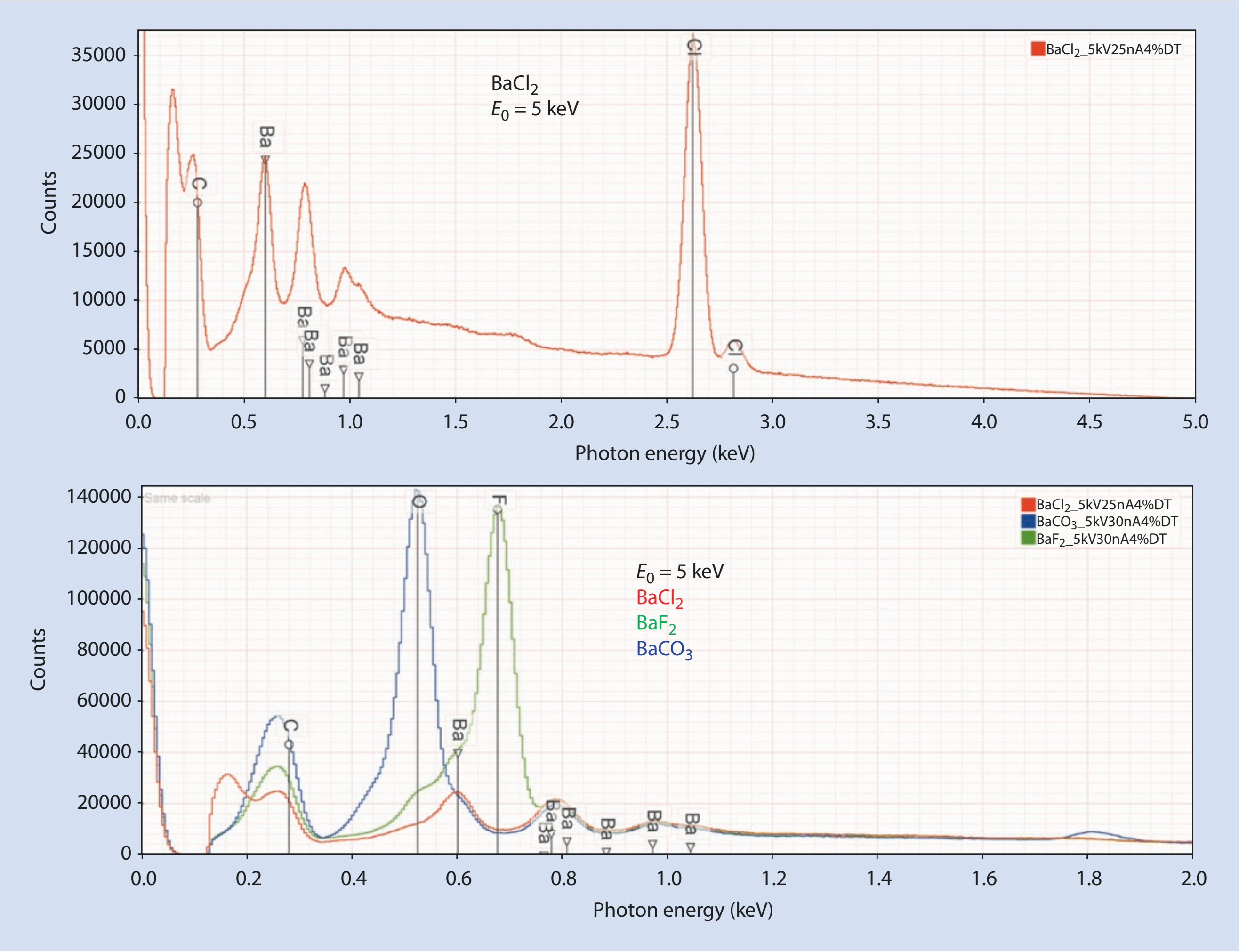

Fig. 22.16 EDS spectrum of barium chloride, showing the Ba M-family (*upper*); EDS spectra of $\mathrm{BaCl_2}$, $\mathrm{BaF_2}$, and $\mathrm{BaCO_3}$ (*lower*); $E_0 = 5$ keV

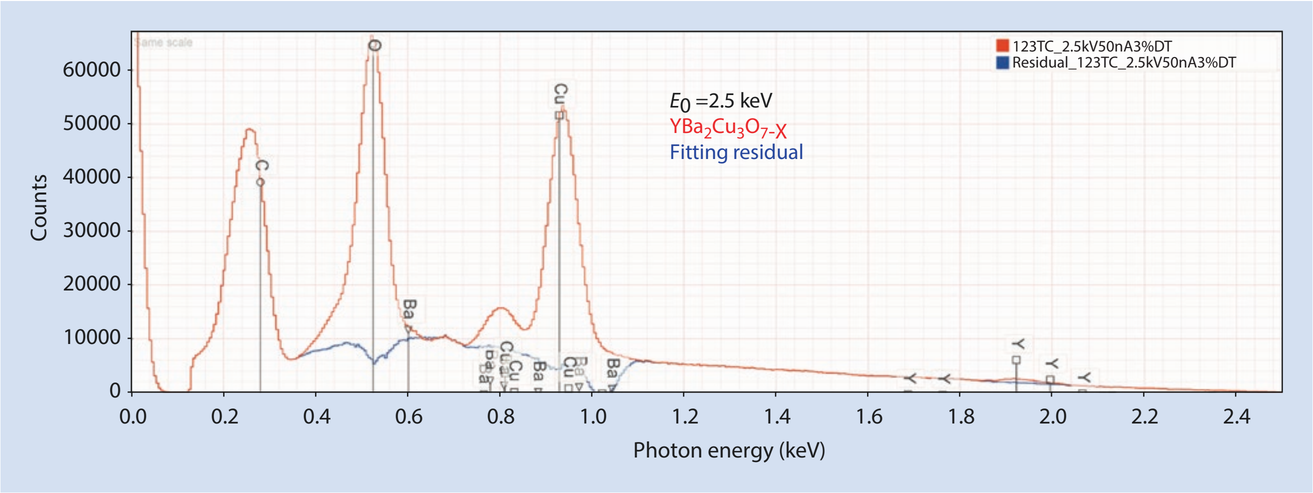

Fig. 22.17 EDS spectrum of $\mathrm{YBa_2Cu_3O_{7-X}}$, and residual after peak fitting for O K-L2, the Ba M-family and Cu L-family; $E_0 = 2.5$ keV

Table 22.5 Analysis of $YBa_2Cu_3O_{7-X}$ at $E_0 = 2.5$ keV

Element	C_{av} mass conc	RDEV %	σ_{rel}, %	C_{av} mass conc	RDEV %	σ_{rel}, %
O	0.1574 (stoich)	−6.4	1.1	0.1787 (ZnO)	6.3	1.3
Cu	0.2910	1.7	3.4	0.3024	5.7	1.4
Y	0.1296	−2.9	3.1	0.1322	−0.90	2.4
Ba	0.4220	2.4	3.6	0.3867	−6.2	2.3

22.3.2 Relative Depth of X-Ray Generation: Susceptibility to Vertical Heterogeneity

Another challenge in low beam energy X-ray microanalysis is that the difference in the depth of generation and sampling of characteristic X-rays from different elements imposes strong requirements on the homogeneity of the specimen along the beam axis. While the physics of characteristic X-ray generation is such that relative differences in the generation and emission of X-rays occur at all beam energies, including the conventional beam energy range, in the low beam energy analysis region the effect is exacerbated due to the rapidly changing range as described by Eq. (22.5). It is useful to consider that the photon energy axis of an EDS spectrum can also be thought of as a range axis that describes the depth to which a given photon energy can be generated. Such a range scale is shown parallel to the photon energy axis in Fig. 22.18 for a ZnS target with $E_0 = 5$ keV. Points on the Kanaya–Okayama range scale corresponding to exciting X-rays with ionization energies of 4 keV, 3 keV, 2 keV and 1 keV are noted. The range scale is non-linear when compared to the energy scale due to the $E_0^{1.67}$ term in the range equation. In ZnS, S K ($E_c = 2.47$ keV) can be excited to a depth of approximately 0.21 µm, while Zn ($E_c = 1.02$ keV) continues to a depth of 0.28 µm. If the ZnS contained Ca as a trace or minor constituent, it would only be generated to a depth of 0.09 µm. Thus, if quantitative analysis is to be successful by means of the k-ratio/matrix corrections protocol performed at a single beam energy in the low beam energy regime, the material must be homogeneous from the surface to the full range of the excited volume.

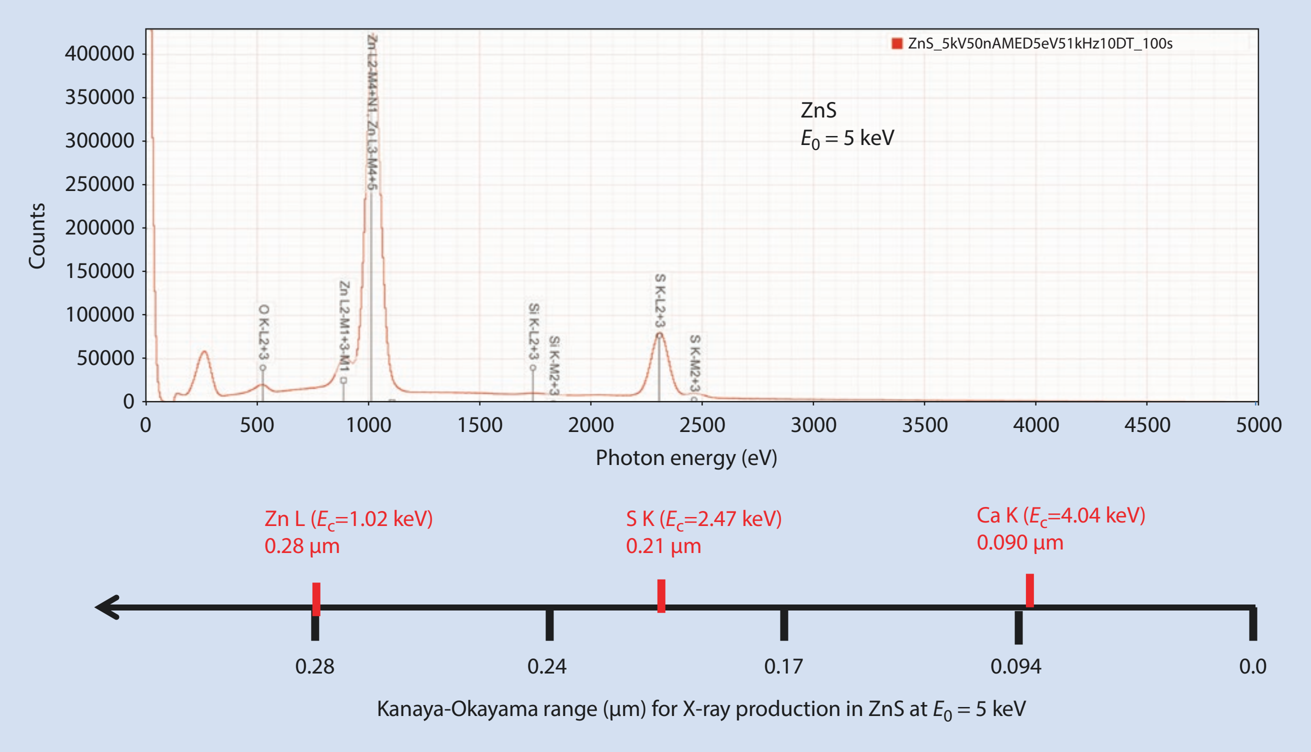

Fig. 22.18 EDS spectrum of ZnS illustrating concept of the energy axis of the spectrum and the corresponding depth of X-ray generation; $E_0 = 5$ keV

22.3.3 At Low Beam Energy, Almost Everything Is Found To Be Layered

Most “pure” elements have surface layers such as native oxide, hydration layers, and others that compromise the requirement for uniform composition throughout the electron-excited volume of both the unknown and the standard(s). For example, when “pure” silicon is used as a standard, the intensity of the O K-$L_{2,3}$ peak, which arises from the SiO_2 layer on Si, increases relative to the Si K-$L_{2,3}$ peak as the beam energy is lowered, as seen in ▪ Fig. 22.19. In conventional analysis with $E_0 \geq 10$ keV, the deviation from “pure” silicon that this surface oxide represents does not constitute a significant source of error since the range is so much greater than the native oxide thickness. However, for low beam energy analysis, the surface oxide constitutes an increasingly significant fraction of the beam excitation volume as the beam energy is reduced, introducing an increasingly larger error because of the uncertainty in the standard composition.

The presence of the O K-$L_{2,3}$ peak from a surface oxide is especially problematic when it interferes with the characteristic peak of interest, such as the Ti L-family, as shown in ▪ Fig. 22.20. O K-$L_{2,3}$ (0.525 keV) is separated from Ti L_1-M_2 (0.529 keV) by 4 eV. Note the large increase in intensity in this region as the beam energy is lowered from 10 keV to 2.5 keV due to the increased contribution from O K-$L_{2,3}$ as the fraction of the interaction volume represented by the surface oxide increases. Obtaining an adequate standard and peak reference for Ti for low beam energy analysis is thus problematic. Even when a compound expected to be oxygen-free such as $TiSi_2$ is selected, there still appears to be excess intensity due to O K-$L_{2,3}$, as shown in ▪ Fig. 22.20. Thus, it may be necessary to use advanced preparation, such as *in situ* ion milling to clean the surface of Ti to reduce the oxygen contribution to the spectrum.

The conductive coating that is applied to eliminate surface charging in insulating specimens becomes more significant as the beam energy is decreased. This effect is illustrated in ▪ Fig. 22.21 for spectra of the mineral benitoite ($BaTiSi_3O_9$) recorded over a wide range of incident beam energies, where the peak for C K-$L_{2,3}$ is barely detectable at $E_0 = 20$ keV but becomes one of the most prominent peaks in the spectrum at $E_0 = 2.5$ keV. The analyst should try to minimize the carbon contribution to the spectrum by using the thinnest acceptable carbon layer, less than 10 nm thick, and it may be necessary to explore the use of ultrathin (~1 nm) heavy metal coatings as an alternative if it is desired to analyze for carbon.

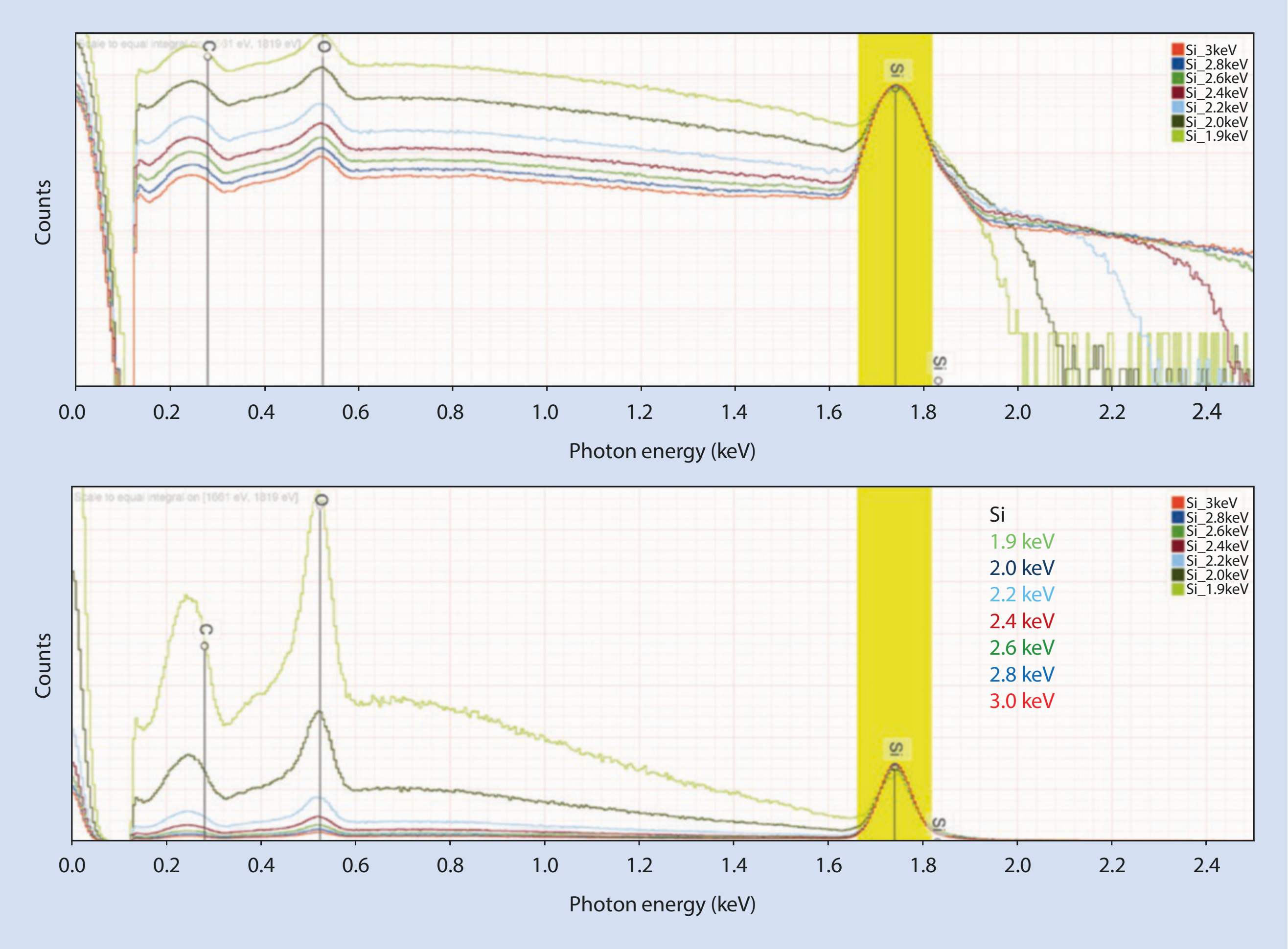

▪ **Fig. 22.19** EDS spectra of Si over a range of beam energies, showing increase in the O K-L_2 peak relative to Si K-L_2; all spectra scaled to Si K-L_2

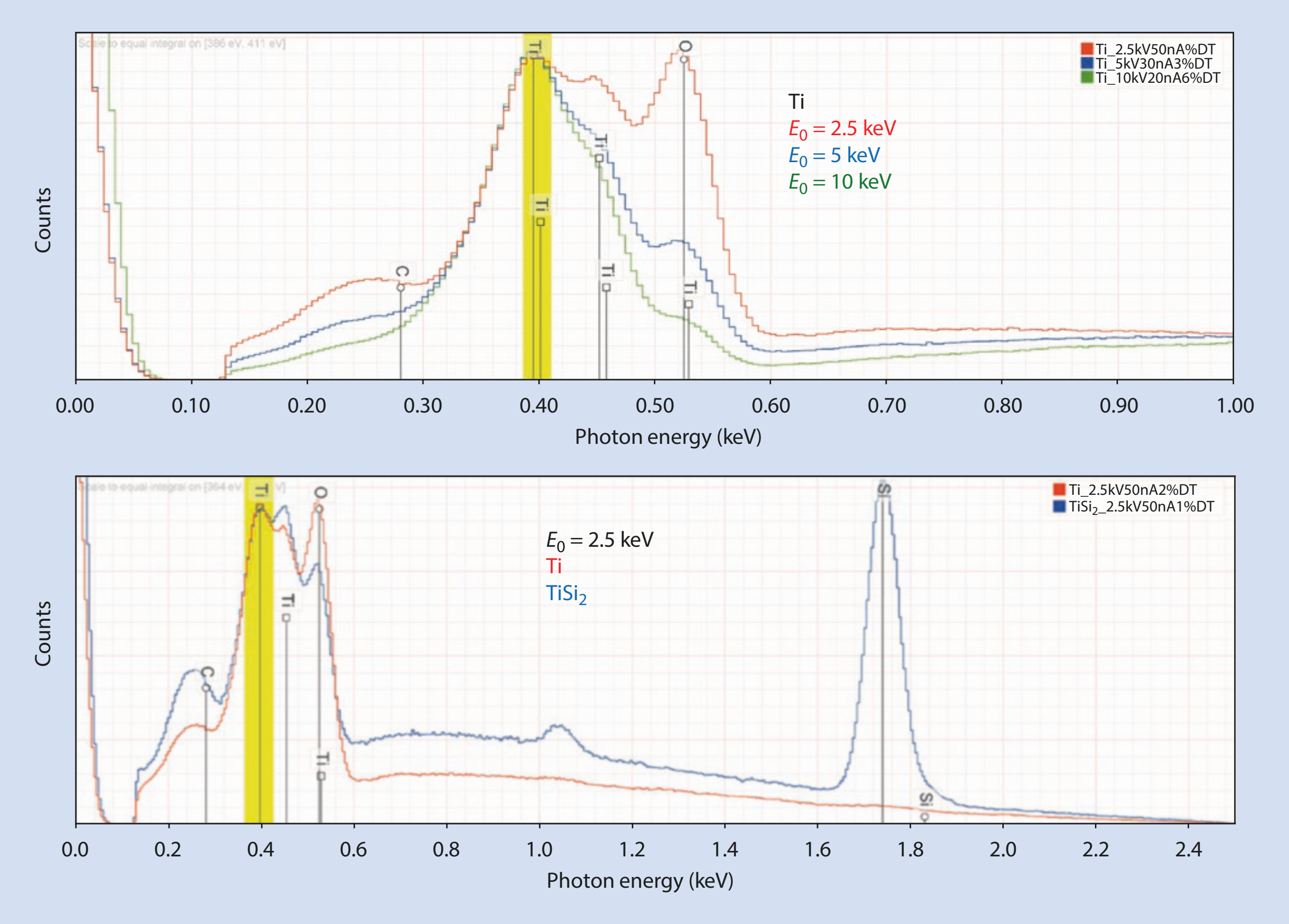

Fig. 22.20 (*Upper*) EDS spectra of Ti at various beam energies showing increase in the O K-L_2 peak relative to Ti L-family peaks; (*lower*) EDS spectra of Ti and $TiSi_2$ at $E_0 = 2.5$ keV

Finding an unexpected composition due to surface modification is a common experience when performing low beam energy analysis of materials that must be analyzed in the as-received condition. Without special surface preparation to expose the interior of the material, such as grinding and polishing or ion beam milling, the modified surface region dominates the analysis. Figure 22.22 (upper spectrum) shows an example of TiB_2, where inspection of the fitting residual after analyzing for B and Ti shows significant peaks for C and O. When these elements are included in the analysis, the fitting residual shown in Fig. 22.22 (lower spectrum) is obtained, showing no further undiscovered constituents. The analysis results presented in Table 22.6 reveal significant concentrations of C and O in the TiB_2. Note the greater variance in the C and O contaminants compared to the B and Ti host elements.

Analysis of Surface Contamination

Low beam energy analysis samples such a shallow near-surface region that unexpected contamination layers can dominate an analysis. This can lead to the confounding situation where the analysis can be correct, but what is being

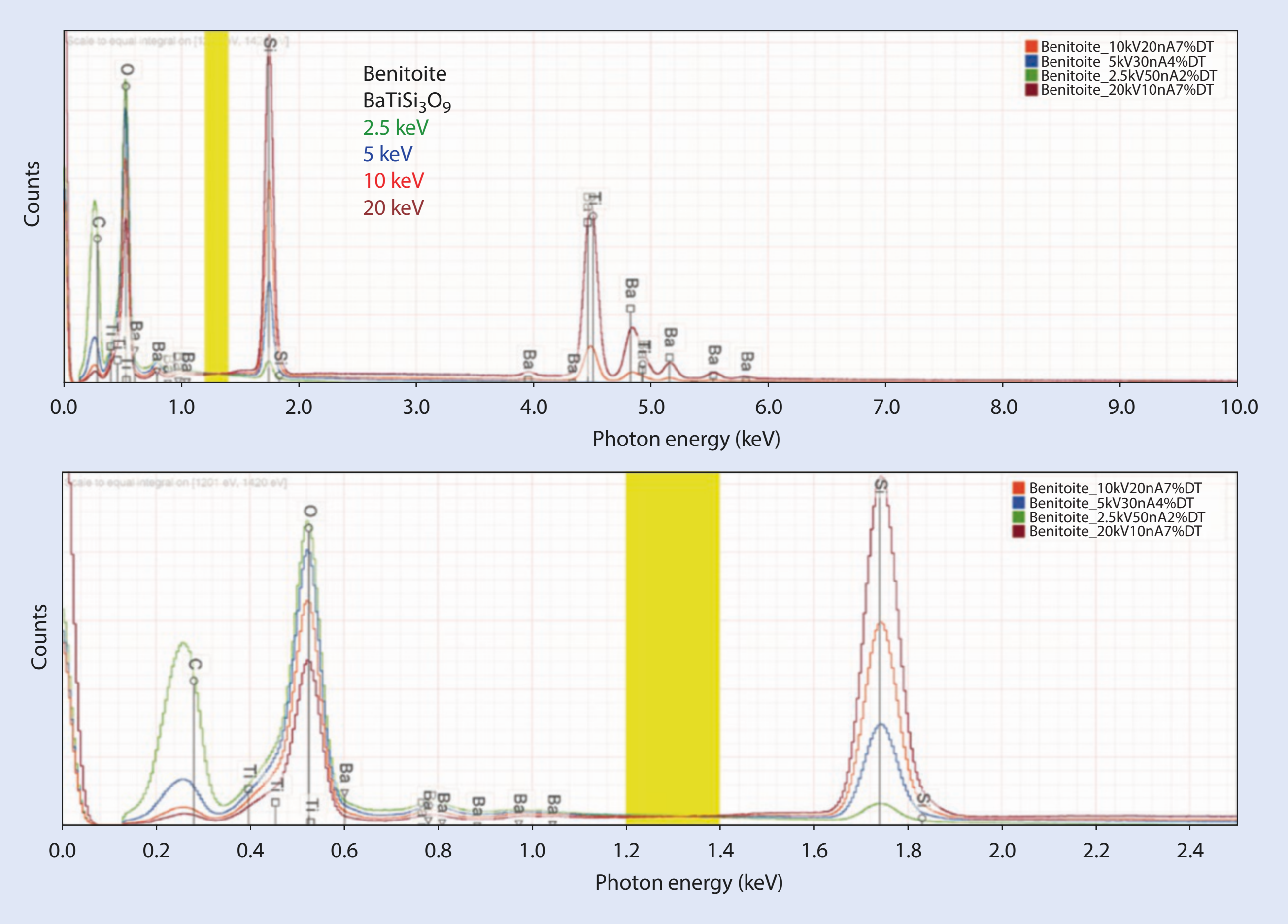

◘ **Fig. 22.21** EDS Spectra of benitoite (BaTiSi$_3$O$_9$) over arrange of beam energies showing relative increase in the C K-L$_2$ peak as the beam energy decreases

measured is unanticipated. An example is shown in ◘ Fig. 22.23, which shows a low beam energy SDD-EDS spectrum of NIST SRM 481 (alloy 20Au-80Ag) where the surface was prepared metallographically more than 30 years earlier. The spectrum shows distinct peaks due to S and Cl from the formation of a surface tarnish layer. Quantitative X-ray microanalysis with DTSA-II confirms the high concentrations of S and Cl and very large RDEV values for Ag and Au, as shown in ◘ Table 22.7a. The specimen mount was re-polished with 0.25-µm diamond abrasive, which eliminated the S- and Cl- rich layer, as seen in the spectrum in ◘ Fig. 22.23. The results of the quantitative analysis after this first repolishing, which are presented in ◘ Table 22.7b, show analytical totals near unity but large RDEV values for Ag and Au, especially for the 20Au-80Ag alloy. This large deviation from the SRM values is likely to be a consequence of the tarnish formation process selectively removing Ag from the alloy. After two additional repolishing steps with 1 µm and 0.25 µm diamond abrasives (◘ Tables 22.7c and 22.7d), this perturbed surface layer was finally removed, exposing the SRM alloy, with the DTSA-II analysis values closely matching the SRM certificate values.

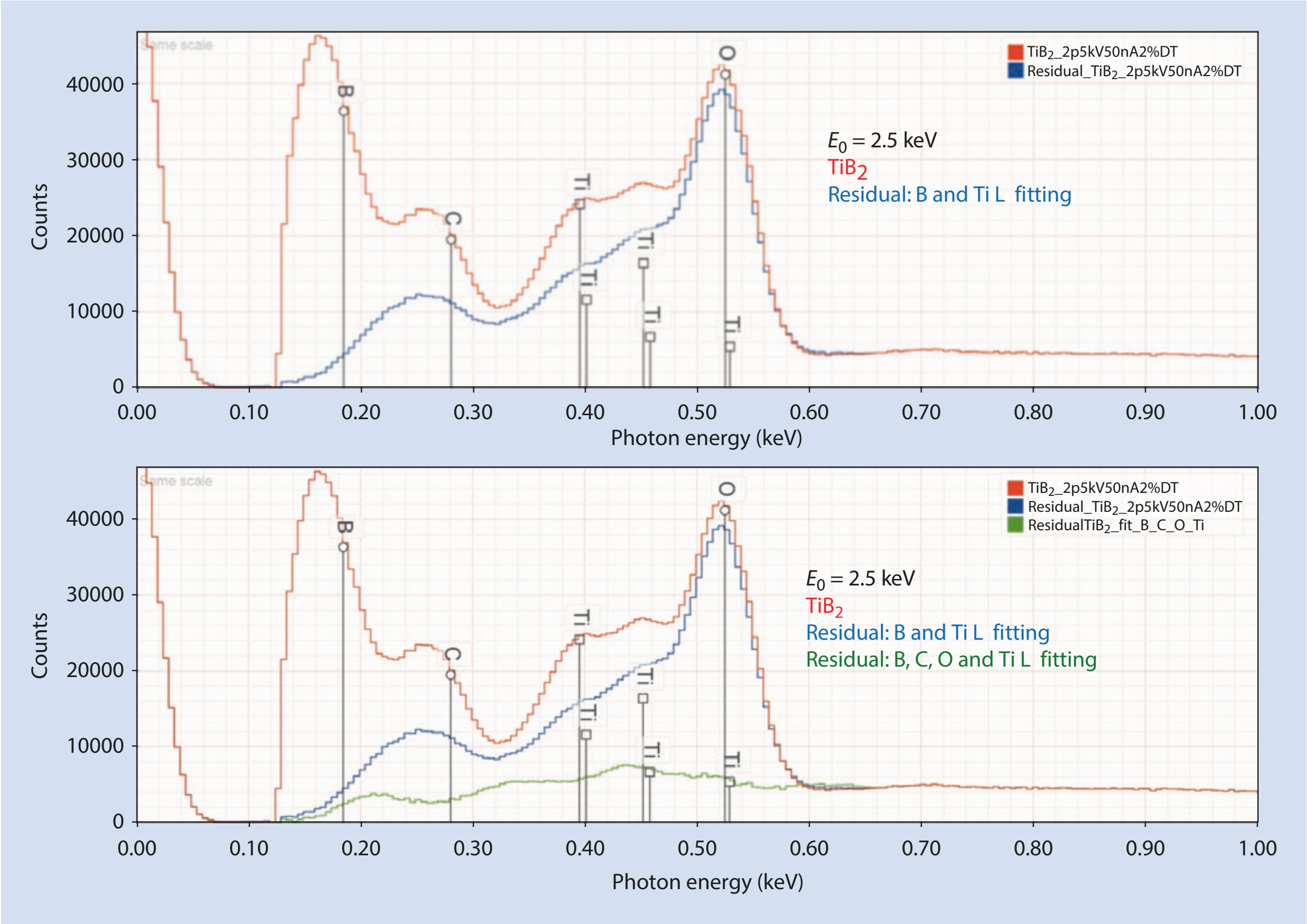

Fig. 22.22 (*Upper*) EDS spectrum of TiB$_2$ and residual spectrum after fitting for B K-L$_2$ and Ti L-family revealing peaks for C K-L$_2$and O K-L$_2$; (*lower*) after fitting for C K-L$_2$and O K-L$_2$; $E_0 = 2.5$ keV

Table 22.6 Analysis of TiB$_2$ at $E_0 = 2.5$ keV

	B (atomic concentration)	C (atomic concentration)	O (atomic concentration)	Ti (atomic concentration)
Mean (5 analyses)	0.5110	0.0708	0.1011	0.3171
σ_{rel}, %	2.7	27	11	2.7

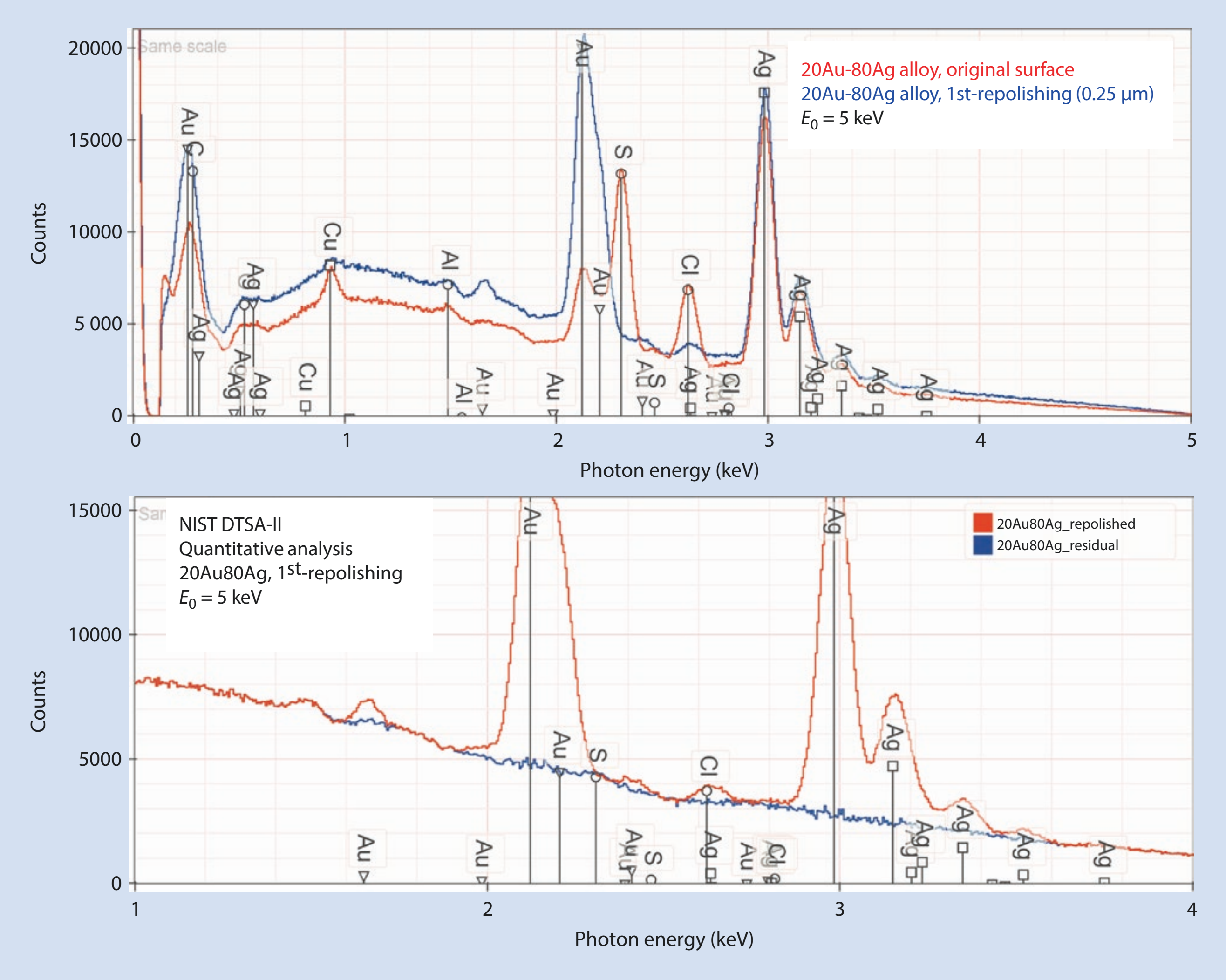

Fig. 22.23 NIST SRM 481 (Au-Ag alloys). Analysis of an old (>30 years) metallographic preparation at $E_0 = 5$ keV, and the spectrum after repolishing with 0.25 µm diamond abrasive

Table 22.7a Analysis of SRM 481 (Au-Ag alloys); 1970s metallographic preparation, original surface; $E_0 = 5$ keV; standards: S (FeS_2); Cl (KCl); Ag, Au

Alloy	Raw analytical total	S (norm mass conc)	σ(%)5 loc	Cl (norm mass conc)	σ(%) 5 loc	Au (norm mass conc)	σ(%)5 loc	RDEV(%)	Ag (norm mass conc)	σ(%) 5 loc	RDEV (%)
20Au–80Ag	0.9855	0.0934	4.4	0.1061	12	0.0796	12	−64	0.7210	0.44	−7
40Au–60Ag	0.9959	0.0311	5.7	0.0965	10	0.3440	6.1	−14	0.5284	2.2	−12
60Au–40Ag	0.9951	0.0094	5	0.045	22	0.5754	4.7	−4.2	0.3706	4.6	−7.2
80Au–20Ag	1.005	0.0051	8.3	0.0365	4.5	0.7340	0.67	−8.3	0.2244	1.6	+12

Table 22.7b Analysis of SRM 481 (Au-Ag alloys); surface after first repolishing with 0.25-µm diamond; $E_0 = 5$ keV; standards: Ag, Au

Alloy	Raw analytical total	Au (norm)	σ(%) 5 loc	RDEV (%)	DTSA-II error budget (%)	Ag (norm)	σ(%) 5 loc	RDEV (%)	DTSA-II error budget (%)
20Au–80Ag	0.9731	0.3050	7.1	+36	0.34	0.6950	3.1	−10.4	0.75
40Au–60Ag	0.9920	0.4460	0.96	+11.4	0.25	0.5540	0.77	−7.6	1.1
60Au–40Ag	0.9907	0.6322	1.0	+5.3	0.21	0.3678	1.8	−7.9	1.5
80Au–20Ag	0.9930	0.8264	0.24	3.2	0.17	0.1736	1.1	−13	2.1

Table 22.7c Analysis of SRM 481 (Au-Ag alloys); surface after second repolishing with 1- and 0.25-µm diamond; $E_0 = 5$ keV; standards: Ag, Au

Alloy	Raw analytical total	Au (norm)	σ(%) 5 loc	RDEV (%)	DTSA-II error budget (%)	Ag (norm)	σ(%) 5 loc	RDEV (%)	DTSA-II error budget (%)
20Au–80Ag	1.005	0.2398	0.87 %	+6.9 %	0.38 %	0.7602	0.28 %	−2.0 %	0.64 %
40Au–60Ag	0.9983	0.4045	0.23	+1.1	0.27	0.5955	0.16	−0.64	0.98
60Au–40Ag	0.9897	0.6084	0.13	+1.3	0.21	0.3916	0.21	−1.9	1.4
80Au–20Ag	0.9998	0.8055	0.26	+0.62	0.19	0.1945	1.1	−2.5	1.9
20Au–80Ag	1.005	0.2398	0.87	+6.9	0.38	0.7602	0.28	−2.0	0.64

Table 22.7d Analysis of SRM 481 (Au-Ag alloys); surface after third repolishing with 1- and 0.25-µm diamond; $E_0 = 5$ keV; standards: Ag, Au

Alloy	Raw analytical total	Au (norm)	σ(%) 5 loc	RDEV (%)	DTSA-II error budget (%)	Ag (norm)	σ(%) 5 loc	RDEV (%)	DTSA-II error budget (%)
20Au–80Ag	1.017	0.2251	0.13	−0.11	0.39	0.7749	0.13	+0.35	0.61
40Au–60Ag	0.9988	0.3909	0.25	−2.3	0.28	0.6091	0.16	+1.6	0.93
60Au–40Ag	0.9931	0.5931	0.12	−1.2	0.22	0.4069	0.18	+1.9	1.4
80Au–20Ag	0.9957	0.7979	0.17	−0.32	0.18	0.2021	0.68	+1.2	1.9

References

Newbury D, Ritchie N (2015) Quantitative electron-excited X-ray microanalysis of borides, carbides, nitrides, oxides, and fluorides with scanning electron microscopy/silicon drift detector energy-dispersive spectrometry (SEM/SDD-EDS) and NIST DTSA-II. Micros Microanal 21:1327

Newbury D, Ritchie N (2016) Electron-excited X-ray microanalysis at low beam energy: almost always an adventure! Micros Microanal 22:735–753